

This is the Title of my Thesis

Johannes Bogen

December 2016

PROJECT THESIS
Department of Physics
Norwegian University of Science and Technology

Supervisor: Professor Antonius T. J. van Helvoort

Preface

Here, you give a brief introduction to your work. What it is (e.g., a Master's thesis in RAMS at NTNU as part of the study program xxx and...), when it was carried out (e.g., during the autumn semester of 2021). If the project has been carried out for a company, you should mention this and also describe the cooperation with the company. You may also describe how the idea to the project was brought up.

You should also specify the assumed background of the readers of this report (who are you writing for).

Trondheim, 2012-12-16

(Your signature)

Ola Nordmann

Acknowledgment

I would like to thank the following persons for their great help during ...

If the project has been carried out in cooperation with an external partner (e.g., a company), you should acknowledge the contribution and give thanks to the involved persons.

You should also acknowledge the contributions made by your supervisor(s).

O.N.

(Your initials)

Summary and Conclusions

Here you give a summary of your work and your results. This is like a management summary and should be written in a clear and easy language, without many difficult terms and without abbreviations. Everything you present here must be treated in more detail in the main report. You should not give any references to the report in the summary – just explain what you have done and what you have found out. The Summary and Conclusions should be no more than two pages.

You may assume that you have got three minutes to present to the Rector of NTNU what you have done and what you have found out as part of your thesis. (He is an intelligent person, but does not know much about your field of expertise.)

Contents

Preface	i
Acknowledgment	ii
Summary and Conclusions	iii
1 Introduction	2
2 Theory	3
2.1 Electron Microscopy	3
2.1.1 Electron-sample interaction	3
2.1.2 Transmission Electron Microscopy (TEM)	4
2.1.3 Scanning Transmission Electron Microscopy (STEM) .	4
2.2 X-ray spectroscopy	4
2.2.1 Energy-Dispersive X-Ray Spectroscopy (EDS)	5
2.2.2 Quantitative X-ray Analysis	6
2.2.3 Thickness estimation	9
2.3 Electron diffraction	10
2.3.1 Diffraction theory	10
2.3.2 Electron diffraction in STEM	12
2.3.3 Scanning Precession Electron Diffraction (SPED) .	12
2.4 Data analysis	14
2.4.1 (Introduction)	14
2.4.2 Template matching	14
2.4.3 Re-binning and rotating multidimensional data	14
3 Experimental	17
3.1 Equipment	17
3.2 Material	17
3.3 Dataset matching	17

3.4	Quantitative analysis	19
4	Results	21
4.1	Dataset matching	21
4.2	Determination of ζ -values	24
4.3	Quantification	25
A	Acronyms	33
B	Additional Information	34
B.1	Introduction	34
B.1.1	More Details	34

Chapter 1

Introduction

Chapter 2

Theory

2.1 Electron Microscopy

In an electron microscope, a beam of electrons are transmitted onto a material. Compared to a microscope using visible light, an EM gives a much higher resolution due to the wavelength of electrons being much smaller than that of visible light. Because of this, an EM can be used to study the atomic structure of materials.

2.1.1 Electron-sample interaction

When the electron beam hits the sample, several different signals are generated. This report will only discuss two of them: Characteristic X-rays (due to inelastically scattered electrons, and elastically scattered electrons. Characteristic X-rays are produced as the incoming electrons interact with inner-core electrons in the sample, and can be used to determine which elements the sample consists of. The theory behind characteristic X-rays, and why they are useful, will be expanded upon in section 2.2. Electrons being transmitted through the sample that are elastically scattered (that is, the energy of the incoming electrons is conserved) gives rise to a diffraction pattern, which can be used to determine the crystallographic properties of the sample. Electron diffraction will be properly introduced in section 2.3 [12].

2.1.2 Transmission Electron Microscopy (TEM)

There are many different kinds of transmission electron microscopes (TEMs), of which only the scanning TEM (STEM), introduced in section ??, will be expanded upon here. Before discussing the STEM, however, the basics behind the TEM will now be presented. In a conventional TEM, a broad, parallel beam of electrons is transmitted through a sample. In order for a sufficient amount of electrons to be transmitted, the sample is required to be thin (a thickness of $<100\text{ nm}$ is common). A TEM typically operates with electron energies of $\approx 200\text{ keV}$ or 300 keV , giving the electrons a velocity $v > c/2$ which requires relativistic effects to be taken into account. Another factor that should be considered is the possibility of the electron beam damaging the material. This can happen as the chemical bonds in the material are broken (radiolysis), atoms are displaced or ejected from the crystal lattice (knock-on damage or sputtering, respectively) or as the material is changed due to heating. [12]

2.1.3 Scanning Transmission Electron Microscopy (STEM)

A scanning transmission electron microscope (STEM) uses an electron beam focused onto a small spot on the sample. The sample is then scanned in a raster pattern and the signal is recorded for each point. This technique can be used to investigate very small areas of the sample and accurately study transitions in atomic structure and/or composition.

2.2 X-ray spectroscopy

The characteristic X-rays resulting from inelastic scattering of the electrons being transmitted through the sample can be used for both qualitative and quantitative analysis. Qualitative analysis can determine which elements are in the sample, while quantitative analysis can indicate the composition of the different elements. When X-ray spectroscopy is performed in a STEM, the electron probe is scanned over the material and focused on each pixel for a certain amount of time. During this time period, the X-rays being emitted

from the sample are detected and the signal for the pixel is saved before the probe moves to the next pixel.

2.2.1 Energy-Dispersive X-Ray Spectroscopy (EDS)

X-ray emission

As previously mentioned, characteristic X-rays are produced due to inelastic scattering of the incoming electrons on the sample. If an electron reaches the inner-shell electrons of an atom in the sample, and a sufficient amount of energy is transferred to the inner-shell electron, the electron will be ejected from the nucleus. That is, it reaches an energy above the Fermi level and is no longer bound to the nucleus [CHECK THIS]. The atom is now in an excited state, and will seek to return towards its ground state. This leads to an electron in an outer shell taking the place of the ejected electron in the inner shell, and in the process emitting an X-ray or an Auger electron (Auger electrons will not be discussed further). If an X-ray is emitted, its energy will be characteristic of the specific element, as different elements have different critical ionization energies. The critical ionization energy is the energy required for an inner-shell electron to be ejected from the nucleus.

There will not necessarily only be emitted one characteristic X-ray for each hole created in the inner shell of an atom. This is because the outer-shell electron filling the hole will create a new hole in its shell, which must be filled by an electron in a shell even further out, and maybe emitting another characteristic X-ray. This process continues until there is a hole in the outermost shell of the atom that can be filled by an electron in the conduction or valence band of the material. The energy of the characteristic X-rays will also depend on which transition it is emitted because of. In addition, due to quantum effects the electron shells might be split into several sub-shells, further increasing the number of different energies the emitted X-rays can have.

The probability for a specific transition to occur must also be taken into account. If a transition between two specific shells has a relatively high probability compared to other transitions in the element, more characteristic X-rays with the corresponding energy will be emitted over a certain time

period. This will lead to higher peaks in the EDS spectrum, which will be discussed shortly.

X-ray detection

When doing EDS in a TEM, an X-ray detector is positioned above the sample to detect the X-rays emitted from it. The detector then measures the energy of each incoming X-ray, with a given energy resolution. If the measurement is done using STEM, the electron probe is scanned over the sample and kept at each pixel for a certain amount of time during which emitted X-rays are detected. When the scanning is complete, this results in a three dimensional EDS spectrum.

EDS spectrum

In an EDS spectrum, the intensity of the X-rays is plotted against the energy of the X-rays. The intensity at a certain energy refers to the number of counts, that is, how many X-rays with that energy that were detected by the detector. An example of an EDS spectrum is shown in Figure 2.1. By consulting a table of known X-ray energies for the emission lines from different elements, for example [1], one can determine which elements are present in the sample. However, knowing which elements are present is not enough to determine the structure of the material. A next step can be to perform quantitative analysis on the same spectrum.

2.2.2 Quantitative X-ray Analysis

Quantitative analysis of an EDS spectrum gives information about the composition of the different elements in the material. A quantitative analysis might result in learning that an unknown material is a compound of a few different elements. In order to determine which compound this is, quantitative analysis is necessary.

There are primarily two methods for quantitative X-ray analysis: The Cliff-Lorimer ratio technique and the ζ -factor method. The basis for both is

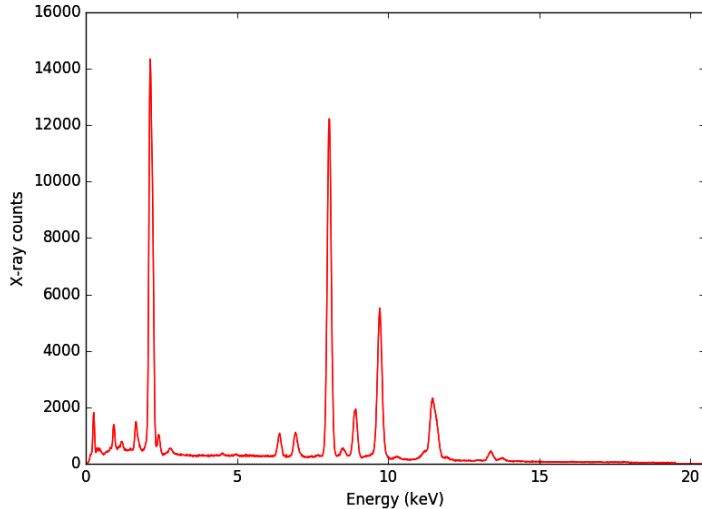


Figure 2.1: Example of EDS spectrum

assuming that the concentration of an element in a material is proportional to the intensity of characteristic X-rays being emitted from it, $C \propto I$.

The Cliff-Lorimer ratio technique

The Cliff-Lorimer ratio technique, first introduced in 1972 [6], assumes that the weight percent ratio of two elements is proportional to their intensity ratio,

$$\frac{C_A}{C_B} = k_{AB} \frac{I_A}{I_B}, \quad (2.1)$$

where C is the weight percent, I is the intensity of the characteristic X-rays and the proportionality factor k_{AB} is called the Cliff-Lorimer factor, or the k -factor. The k -factor depends not only on the properties of the elements A and B , but also on the instruments used, the conditions under which the experiment was done, and how the intensities are extracted from the spectrum. This technique has several drawbacks: Firstly, determining the k -factor experimentally is very time-consuming, but a theoretical calculation can have a severe error [12]. And secondly, the multi-element thin standards necessary for experimental determination are difficult to prepare.

The ζ -factor method

The ζ -factor method was introduced by M. Watanabe and D. B. Williams in 1996, and overcomes several of the problems with the Cliff-Lorimer technique. If the material is a thin-film, its mass-thickness can be assumed to be proportional to the intensity of the characteristic X-rays I and the composition C ,

$$\rho t = \zeta \frac{I}{CD_e}, \quad (2.2)$$

where ρ is the density of the material, t is its thickness and D_e is the total amount of electrons that hit the material during the measurement.

Using the thin-film approximation to find a theoretical expression for the intensity I , the proportionality factor ζ can be found to be

$$\zeta = \frac{M}{N_v Q \omega a [\Omega/(4\pi)] \epsilon}. \quad (2.3)$$

Here, M is the atomic weight, N_v is Avogadro's number, Q is the ionization cross section, ω is the fluorescence yield, a is the relative transition probability, $\Omega/(4\pi)$ is the detector collection-angle and ϵ is the detector efficiency [8]. If the composition and thickness of a material is known, equation (??) can be used to calculate the ζ -factor for the material.

Another advantage of the ζ -factor method is the inclusion of absorption correction. The absorption correction-term for a specific X-ray line is given as

$$A = \frac{(\mu/\rho)_{sp} \rho t \text{cosec}(\alpha)}{1 - \exp[-(\mu/\rho)_{sp} \rho t \text{cosec}(\alpha)]}, \quad (2.4)$$

where (μ/ρ) is the mass absorption coefficient for the specific X-ray line, and α is the X-ray take-off angle. Absorption correction is implemented by multiplying this term to the intensity I in Eq. (2.2), giving

$$\rho t = \zeta \frac{I}{CD_e} A \quad (2.5)$$

In a multi-element system, assuming the compositions obey $\sum_j C_j = 1$, Eq. (2.2) gives the mass-thickness and composition of each element as

$$\rho t = \sum_j \frac{\zeta_j I_j A_j}{D_e}, \quad C_i = \frac{\zeta_i I_i A_i}{\sum_j \zeta_j I_j A_j} \quad (2.6)$$

These equations can be solved through an iterative process: First, the mass-thickness and compositions are determined without absorption correction. Then the correction terms are calculated, and the mass-thickness and compositions are calculated with absorption correction. These last two steps are repeated until convergence is reached [8].

As both the ζ -factor and the k -factor in Eq. (2.2) and ?? are proportional to the X-ray intensity and composition, the ratios for two elements should be roughly equal,

$$\frac{\zeta_A}{\zeta_B} \approx k_{AB} = \frac{k_{AX}}{k_{BX}}, \quad (2.7)$$

where X denotes the element which the k -values have been measured with respect to.

2.2.3 Thickness estimation

The thickness of a sample can be estimated by using electron energy-loss spectroscopy (EELS), in which the energy which electrons lose due to inelastic scattering is measured. From Poisson statistics, the mean number of scattering events for each electron can be calculated from the EELS spectrum as

$$t/\lambda = \ln(I_t/I_0), \quad (2.8)$$

where I_0 and I_t are the areas under the zero-loss peak and under the whole spectrum, respectively. If the mean free path λ is known, the thickness t can be estimated [4, 11].

2.3 Electron diffraction

When electron diffraction is performed in a TEM, a beam of electrons is transmitted through the specimen. As the electrons pass through, some are scattered due to the atomic potentials in the specimen. By detecting the positions of the electrons after they have been transmitted through the specimen, a diffraction pattern is obtained. Analyzing this diffraction pattern can determine the characteristics of the specimen, for example whether it is crystalline or amorphous, if there are several phases present, and if crystalline, what its crystallographic characteristics are. This information can not be obtained through EDX.

Electron diffraction in a STEM, or scanning electron diffraction (SED) works similarly to EDX in STEM: A parallel electron probe is scanned over the specimen in a raster pattern, and the resulting 2-dimensional diffraction pattern is recorded for each pixel. The result is a 4-dimensional dataset: Two axes in real space and two in reciprocal space.

2.3.1 Diffraction theory

When discussing the diffraction of electrons, it is convenient to regard the electrons as waves. When a parallel electron wave with a wave vector \vec{k}_i reaches the specimen, the electrons will scatter to different angles θ . Assuming the scattering is purely elastic, i.e. the energy of the electrons is conserved, the wave vectors of the scattered electrons will be equal in magnitude to the wave vector of the incoming electrons, $|\vec{k}_s| = |\vec{k}_i| = {}^1\lambda$.

+++ figure here

?? shows two electrons being scattered from atoms at two different atomic planes separated by a distance d . After being scattered, the distances the electrons have traveled differs by $2d \sin \theta$, where θ is the scattering angle. If this path difference is equal to an integer number of wavelengths, the electrons' phases will be equal. The angles θ where this occurs are called the Bragg angles, and this condition is called Bragg's law, given by

$$2d \sin \theta_B = N\lambda, \quad (2.9)$$

where N is an integer.

The equivalence of Bragg's law in reciprocal space is the Laue condition. In order to discuss this, a few definitions must be made. First of all, the scattering vector $\vec{Q} = \vec{k}_s - \vec{k}_i$ describes the change in the wave vector due to diffraction. The resulting phase difference between the two scattered electrons can thus be written as $\Delta\phi = \vec{R} \cdot \vec{Q}$, where \vec{R} gives the position of the second atom relative to the first. To generalize this, note that any three-dimensional lattice can be described by a set of vectors

$$\vec{R}_n = n_1 \vec{a}_1 + n_2 \vec{a}_2 + n_3 \vec{a}_3, \quad (2.10)$$

where the vectors \vec{a}_i are called the lattice vectors, and n_i are integers. If the phase difference is to be equal to zero, so that Bragg's law (Eq. (2.9)) is fulfilled, we get the condition

$$\vec{R}_n \cdot \vec{Q} = 2\pi N, \quad (2.11)$$

where N is an integer. To solve this equation, let us first define the reciprocal lattice. Similarly to the definition of the real-space lattice in Eq. (2.10), the reciprocal lattice can be defined as

$$\vec{G}_{hkl} = h\vec{a}^*_1 + k\vec{a}^*_2 + l\vec{a}^*_3, \quad (2.12)$$

where h , k and l are integers, and the vectors \vec{a}^*_i satisfy the condition

$$\vec{a}^*_i \cdot \vec{a}_j = \delta_{ij},$$

where δ is the Kronecker delta. It is now seen that the reciprocal lattice vectors \vec{G} satisfy Eq. (2.11), as the scalar product $\vec{G} \cdot \vec{R}_n$ is an integer. The Laue condition can now be written as

$$\vec{Q} = \vec{G} \quad (2.13)$$

In other words, there will be constructive interference only when the scattering vector \vec{Q} equals a reciprocal lattice vector \vec{G}_{hkl} .

The Laue condition can be visualized through the Ewald sphere construction. Section 2.3.1 shows the reciprocal lattice, the wave vectors of the incoming

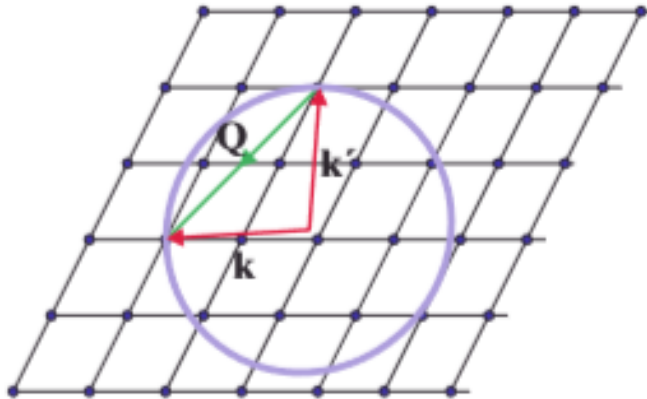


Figure 2.2: Ewald sphere. From Modern x-ray physics.

and the scattered waves, and a circle with radius $|\vec{k}_i| = \lambda^{-1}$. The incoming wave vector \vec{k}_i terminates on a reciprocal lattice point, which is where the diffracted wave vector \vec{k}_s originates. \vec{k}_s can terminate anywhere on the Ewald sphere, but the Laue condition will be satisfied only if it terminates on a lattice point.

2.3.2 Electron diffraction in STEM

2.3.3 Scanning Precession Electron Diffraction (SPED)

Scanning precession electron diffraction (SPED) is a modification of SED. Fig. 2.3 shows the schematic of SPED. The electron beam is now tilted a fixed angle ϕ and precessed around the vertical axis. The beam will hit the sample at the same spot during the precession; only the direction of the incoming beam will be changed. The diffracted beam is also precessed so that the locations of the diffraction spots remain fixed during the precession.

There are several reasons why adding precession to electron diffraction gives better results. The perhaps most important is that the Ewald sphere is precessed in reciprocal space. This causes the Laue condition to be fulfilled for

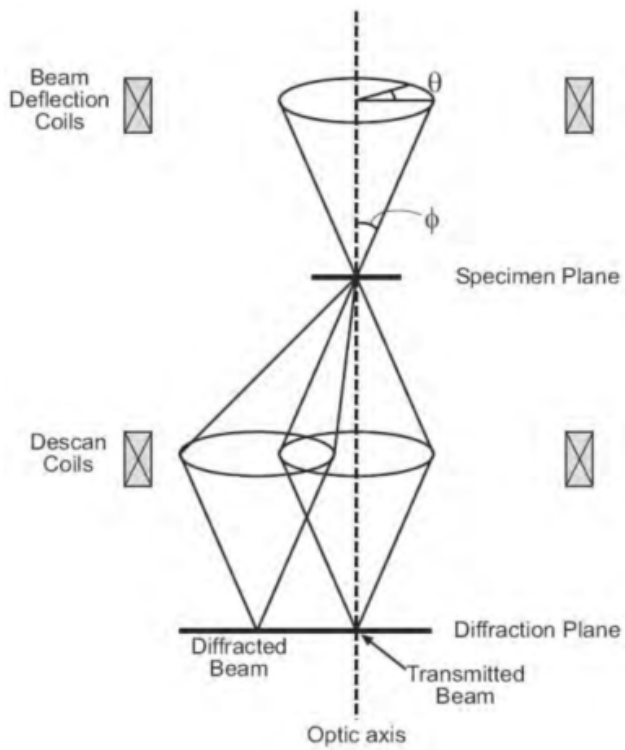


Figure 2.3: Figure from [10]

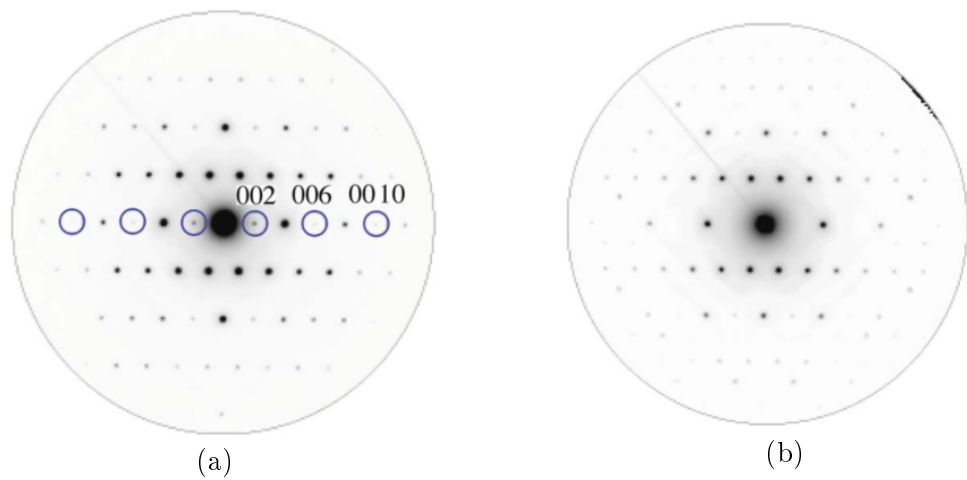


Figure 2.4: From [12]

a higher number of reciprocal lattice points, resulting in more visible spots in the diffraction pattern. Another major improvement is the reduction of dynamical effects, in particular double diffraction, in the diffraction pattern. Double diffraction occurs when an electron is scattered twice, and can result in diffraction spots appearing even though they do not satisfy the Laue condition. As the beam is being precessed, dynamical effects are to a large extent averaged out [12, 10]. Fig. 2.4 shows an example of how using a larger precession angle causes a reduction of dynamical effects.

2.4 Data analysis

2.4.1 Template matching

Template matching is used for finding the location in a reference image where a template image fits best. The function *MatchTemplate* in the python library OpenCV does this by sliding the template image over the reference image, and recording how well it fits at each point. This matching value is given as the normed square difference between the two images for each pixel in the reference image:

$$R(x, y) = \frac{\sum_{x',y'} (T(x', y') - I(x + x', y + y'))^2}{\sqrt{\sum_{x',y'} T(x', y')^2 \cdot \sum_{x',y'} I(x + x', y + y')^2}} \quad (2.14)$$

Here, (x, y) are the coordinates of the reference image, (x', y') the coordinates of the template, $I(x, y)$ is the value of the pixel (x, y) in the reference image and T likewise in the template. The matching value $R(x, y)$ can take any value between 0 and 1, where 0 means a perfect match and 1 a perfect mismatch.

2.4.2 Re-binning and rotating multidimensional data

Attempting to re-bin and rotate a multidimensional array can be problematic. A rotation that is not a multiple of 90 degrees will lead to jagged edges, and zero-values will have to be added to make it rectangular again. An even

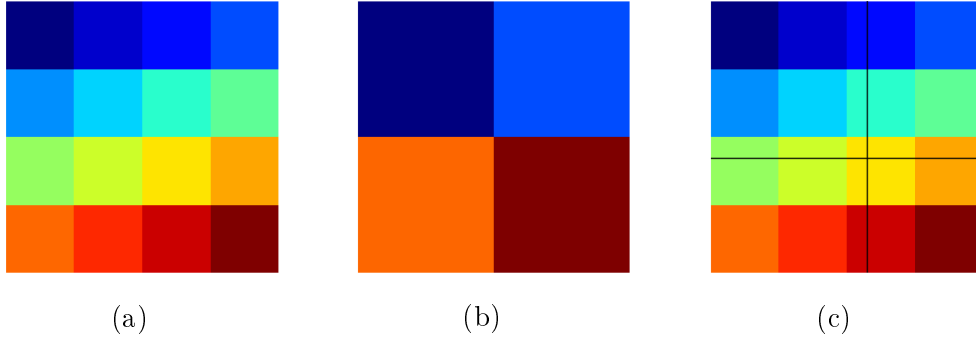


Figure 2.5: Rebin figures

bigger problem occurs when re-binning an array. If the new lengths along each axis are divisors of the original lengths, it is relatively easy. Fig. 2.5(a) shows a 4x4 array, where each value is visualized by a color. Rescaling this array by a factor of $s = 2.0$ is simple as each value in the new array can be calculated as the mean of the corresponding 4 values (2x2 array) in the original array, resulting in the array in Fig. 2.5(b). This is called down-sampling, and causes information to be lost. Likewise, if re-binning the 4x4 by a factor of $s = 0.5$, each value in the original array now corresponds to four values (2x2) in the new 8x8 array. These four values can simply be given the same value as the one in the original array. This procedure is called up-sampling, and new information is added.

However, if the new lengths of the array are not divisible by the original lengths, the re-binning procedure is no longer as easy to conceptualize. Imagine that instead of a two-dimensional array we now have a 3-dimensional one, where two of the dimensions are in real space and the third in signal space. This is the format of EDX data taken in STEM mode. Rescaling the real-space axes of this array will necessarily also change the signal axis. One way to solve this problem is to linearly interpolate the signal. Let the array in Fig. 2.5(a) now denote the EDX dataset, with each color representing an EDX spectrum. If it is down-sampled by a scale factor of for example $s = 2.3$, it will become a 2x2 array as before. However, as shown in Fig. 2.5(c), it is no longer as trivial. The top left value will now consist of the sum of the 2x2=4 top left values in the original matrix, plus 30 percent of the 3rd row and column. In the same way, the bottom right value will be the sum of the 2x2=4 bottom right values in the original matrix, plus 70 percent of the

3rd row and column. The result will be similar to Fig. 2.5(b), except that the colors (or spectra) will be slightly different. This process is called linear re-binning.

Chapter 3

Experimental

3.1 Equipment

3.2 Material

3.3 Dataset matching

Several methods were attempted in order to match the SPED and EDX datasets. The goal was that the matching would be performed automatically with no human input. For this to happen, the code would have to scale, rotate and translate one of the the datasets so that it fit the other. The EDX dataset taken at the intersection of the nanowire and the other elements deposited on it shows a relatively clear separation, and is also the dataset covering the biggest area of the sample. As the SPED dataset was taken over a larger area than the EDX dataset, it was decided to attempt to locate the position of the EDX dataset in the SPED dataset.

The python library OpenCV contains an algorithm which uses template matching, described in Section 2.4.2, to find the best matching location of one image in another. The algorithm requires that the images are correctly scaled and rotated. To be used with this function, the two datasets first had to be processed to make them look more similar, and to enhance the border

of the nanowire. The signal space of each of the datasets was limited to only include signals corresponding to the nanowire. For the SPED dataset, this was done by inserting a virtual annulus that covered only one diffraction spot, which was unique for the nanowire. Similarly, in the EDX dataset, the spectrum was cropped to only include the characteristic K_{α} -peaks of Ga and As. The signal dimension of the datasets were then averaged out, in order to convert them into 2-dimensional arrays, or equivalently, gray-scale images.

The images were now rotated and rescaled. The rotation angle was estimated by selecting two points along the same straight line in both images and finding the angle between them. In the HyperSpy metadata of each of the datasets, a scaling factor giving the size of each pixel was given. The SPED image was rotated through the estimated angle, and the EDX image was rescaled by the ratio between the scaling factors. In order to limit the error caused by manual estimation of the rotational angle, the template matching algorithm was run 100 times for angles in the range $\pm 3\%$ of the manually estimated angle. In addition, because the contrast levels of the two images are not necessarily equal, the SPED image was multiplied by a gray-scale factor, ranging from 0.80 to 0.85 (this range was found experimentally to give the best results) through 30 steps.

For each of the 30×100 iterations of the template matching algorithm, the matching value defined in Eq. (2.14) was calculated, and the angle and gray-scale factor giving the lowest matching value were obtained. As it was noticed that the scaling factors in the metadata appeared to be a bit off, making the EDX image slightly larger than it should be. A second iteration was therefore performed, in which also the scale factor was multiplied by a factor ranging from 0.90 to 1.0. For this attempt, a filter was also applied to the EDX image to reduce the brightness of the less bright area surrounding the bright nanowire. If this was not done, the matching algorithm made the EDX image considerably smaller than it should be. The algorithm was now iterated over 50 times for angles, 50 times for the scaling factor and 15 times for the contrast level.

After finding the position of the EDX image in the SPED image, the full datasets were processed to enable them to share the same navigation window (define this?). First, the SPED dataset was rotated using T. Aarholt's *rotate*-function [2], which is currently awaiting implementation into HyperSpy. Then, the EDX dataset was rescaled and re-binned using K. MacArthur's

function *linear_bin* [9], also awaiting implementation into HyperSpy. The functionality of this function is described in Section 2.4.3. Lastly, a portion of the SPED dataset, corresponding to the location of the EDX image found earlier, was cut out. The two datasets now have the same number of pixels in real space, and each pixel corresponds to the same area of the sample. Using the *Mirror navigation*-function in HyperSpyUI [5], the two datasets can be made to share a navigation window.

It then remained to do this for the remaining datasets, all of which were smaller than the dataset used above. Instead of repeating the procedure, the HAADF image, which shows a large area of the sample, was used to find the positions of the remaining datasets with respect to the first. To do this, OpenCV template matching was used to locate the positions of all the datasets in the HAADF image. It was first attempted to use the EDX datasets, converted to images using the technique described earlier. This worked well for the datasets covering a relatively large region of the sample, but not for the smaller ones. Therefore, instead of the datasets, the survey images were used. These images are taken before the EDX recording, and shows a larger region of the sample (is this survey image also HAADF?). After image matching was complete, the matched region was cropped to the actual area of the EDX dataset. The coordinates of this area were found in the survey image's metadata in HyperSpy.

Lastly, the positions of the remaining datasets had to be found in the SPED dataset. The datasets were again scaled and re-binned to fit the SPED dataset, but now also the coordinates in the HAADF image had to be scaled to the SPED dataset, so that the correct area could be cropped out. This step has not been completed.

3.4 Quantitative analysis

The first step in the quantitative analysis was to determine the ζ -factors of the elements in the sample. As this method had not yet been implemented into HyperSpy [3], the necessary code was acquired from the Master's thesis of A. Garmannslund [7]. The thickness of the material was estimated using a thickness map (see Section 2.2.3). Background subtraction was performed by selecting an area of the background signal at both sides of each characteristic

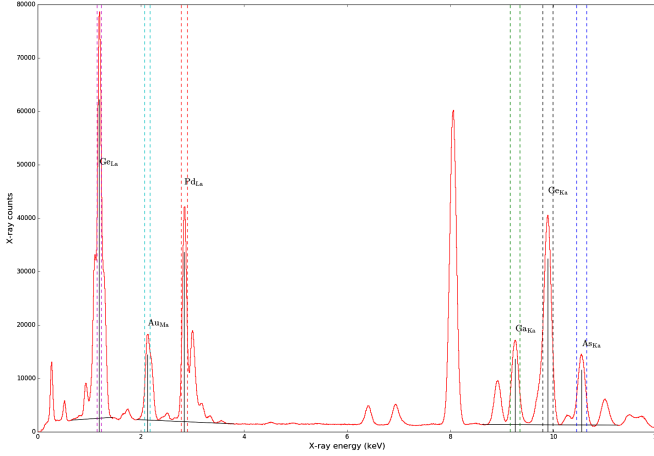


Figure 3.1

line, and drawing a line between the centers of these two areas. The intensities of the lines were then calculated by integrating over the peaks within an integration window of 1.2 FWHM. Fig. 3.1 shows the characteristic X-ray peaks that have been used, the background that has been subtracted, and the integration windows.

The thickness of the sample was estimated using Eq. (2.8). From an EELS map of the unheated sample, the average number of scattering events was found for the middle part of the nanowire. For the mean free path for GaAs, $\lambda = 103$ was used [7].

The quantification of the samples was performed using three different methods: The Cliff-Lorimer ratio technique, for which the necessary k -factors were obtained from the TEM software, the ζ -factor method and the ζ -factor method with background subtraction. HyperSpy was used for the first two of these methods, but absorption correction is at the time not been included in the software. The necessary code for this was also acquired from Garmanlund's thesis. All three techniques were used, in order to enable the results to be compared against each other. To verify the techniques, they were first used on the untreated sample whose composition is assumed to be known. They were then used on the heated sample in order to determine the composition at locations of interest.

Chapter 4

Results

The results will be introduced in the same order as the experiments were conducted. First, the results of matching of one of the EDX datasets with the SPED dataset will be presented. This is followed the position matching of the various EDX datasets with the overview images. Lastly, the calculated ζ -factors and the quantification of the samples using the ζ -factor method and the Cliff-Lorimer technique are displayed.

4.1 Dataset matching

Fig. 4.1 shows the results of matching the largest EDX dataset with the SPED dataset. Fig. 4.1(a) shows the first result, with the SPED dataset rotated by the manually estimated angle, and the EDX dataset scaled using the scale factor obtained from the metadata. In Fig. 4.1(b), the angle has been iteratively optimized, and therefore increased by 0.4%. Fig. 4.1(c) shows the third result, where both the rotation angle and the scale factor has been optimized, and the EDX image has been filtered to include less of the melted region. This led to an increase in the angle of 2.8% from the manually estimated one, while the scale factor was reduced by 7%. Should processed images be shown as well?

The results from locating the EDX datasets in the HAADF overview images are displayed in Fig. 4.2(a) and ?? for the non-treated and the heat-treated

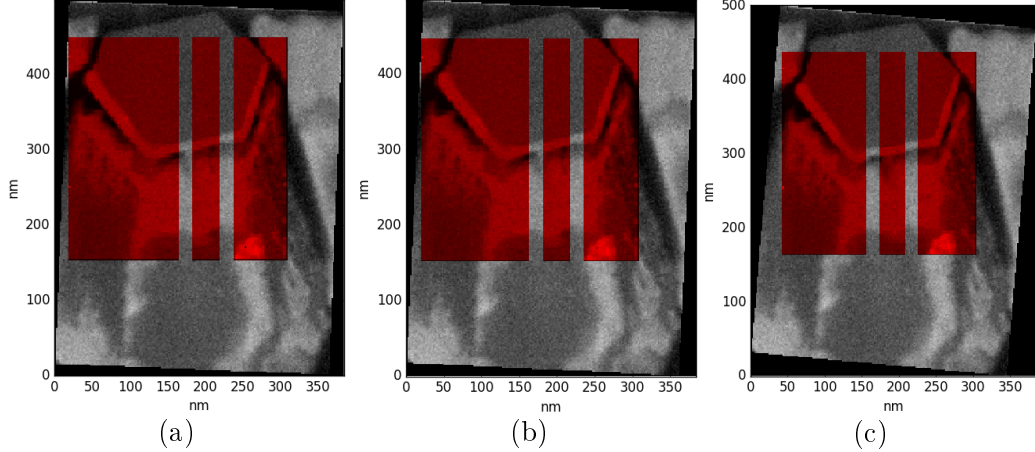
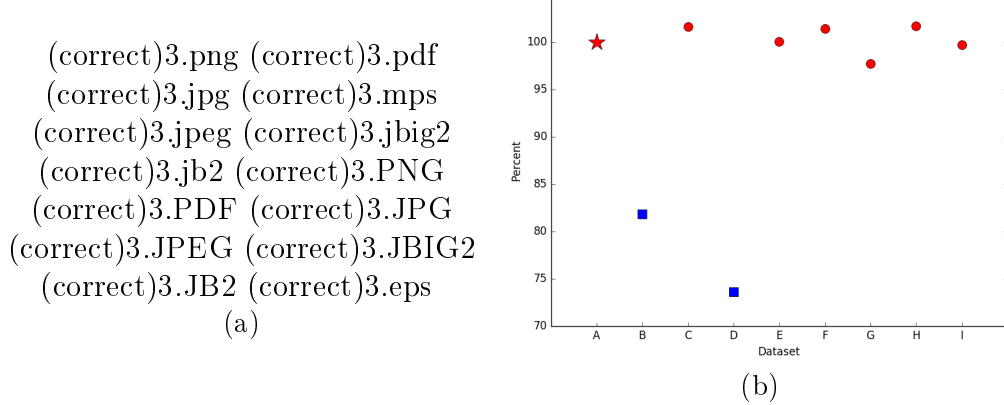
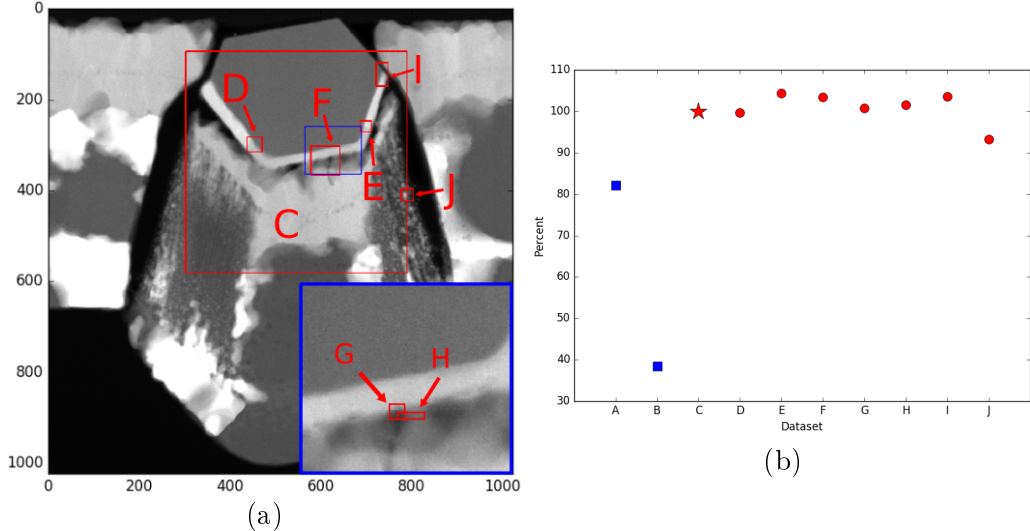


Figure 4.1: Caption



samples, respectively. In the non-treated sample, the two datasets B and D were not correctly located in the overview image. The calculated location of dataset B was completely off, while the position of D was just slightly offset. The actual positions of these datasets were estimated by eye and marked in Fig. 4.2(a) as blue dotted rectangles. The rest of the datasets were located correctly, and their positions are shown as red rectangles. For the heat-treated sample, all the datasets that were included in the overview image were correctly located. However, the areas covered by two the datasets A and B were found to not be included in the overview image.

The accuracy of the matching for the different datasets are shown in Fig. 4.2(b)



for the non-heated sample, and in Fig. 4.3(b) for the heated values. The horizontal axis shows the different datasets while the vertical axis is the matching value in percent, where 100 % is defined to be the matching value of the dataset covering the biggest area in each respective sample. The matching of this dataset is assumed to be the most trustworthy due to there being fewer potential locations that resemble the actual location, as there are several distinct features. For the smaller datasets, or more accurately, the datasets with smaller survey images, there might be several different locations in the overview image that all give a fairly good match.

In both figures, the red star is the value of the dataset used as reference, the red circles are the correctly matched datasets while the blue squares are the datasets that resulted in a wrong location. The non-heated sample (Fig. 4.2(b)) shows high values for all the correctly located datasets, and significantly lower values for the wrongly located ones. In addition, it must be noted that the exact location of dataset F was impossible to verify visually due to the survey image not being large enough to distinguish specific features. In the heated sample (Fig. 4.3(b)), all the red correctly located datasets have high values while the datasets that were not present in the reference image have distinguishably lower values.

4.2 Determination of ζ -values

The calculated ζ -values for all the characteristic X-ray lines used to quantify the data are presented in Table 4.1, along with which dataset was used to calculate them. The calculated ζ -values were compared to the corresponding k -values using Eq. (2.7), with $\text{Ga}_{K\alpha}$ as reference element. Fig. 4.4 shows the results, with the mean value and spread of the ζ -factors indicated. The average ζ -values have been used for all further calculations.

Table 4.1: zeta values

Element (X-ray line)	Dataset	ζ -value
Ga (K_α)	C*	582
Ga (K_α)	A	608
As (K_α)	C*	689
As (K_α)	A	706
Ge (K_α)	B	732
Ge (K_α)	D	741
Ge (K_α)	A	748
Ge (L_α)	A	933
Ge (L_α)	D	900
Ge (L_α)	B	900
Pd (L_α)	E	1248
Pd (L_α)	A	1284
Pd (L_α)	B	1318
Au (M_α)	B	2397
Au (M_α)	C	2387

4.3 Quantification

This must be written better. But where should it come? Experimental, results or discussion? The choice of which characteristic peaks to use for different areas in the sample needs to be addressed first. First of all, the Ge_K α -peak has a significant overlap with the Au_L α -peak, which is why the Au_M α -peak was used. Secondly, when attempting to calculate the

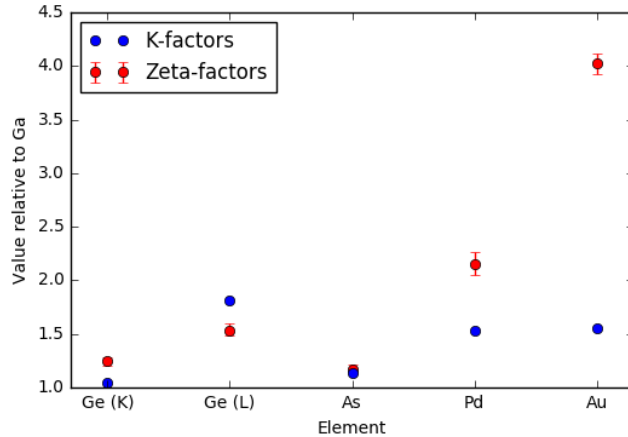


Figure 4.4: zeta - k - comparison

composition of Ga and As simultaneously with Au, the results were very bad. Thirdly, if measuring the composition of Ga and As simultaneously with Ge, using the Ge_L α -peak, all three techniques said there was 10% Ge in the area known to consist of only Ga and As. This did not happen while using the Ge_K α -peak. To conclude, when measuring elements Ga, As, Ge and Pd, the Ge_K α -peak was used, but when measuring elements Ge, Pd and Au, the Ge_L α -peak was used.

Figs. 4.5 and 4.6 shows the compositions of two areas (Figs. 4.5(a) and 4.6(a) shows the locations of these areas) in the untreated sample, as calculated using the Cliff-Lorimer ratio method (CL method) and the ζ -factor method with and without absorption correction. All the spectra have been averaged in the horizontal direction. The results are as expected. Figs. 4.5(b) and 4.5(c) shows that the nanowire consists of Ga and As in a 50/50 ratio, and Figs. 4.5(d) and 4.5(e) shows that the next two layers are approximately 100% Pd and Ge. In the second area, Figs. 4.6(b) to 4.6(d) shows that the composition of elements are approximately 100% Au in the top region, 100% Pd in the middle and 100% Ge in the lower region.

All three techniques give fairly similar answers for Ga and As, while the differences between the CL- and ζ -factor methods are significantly higher for Pd, Ge and Au. The inclusion of absorption correction does not give very different results for any of the elements, except for the Ge-region in the

second area where the absorption correction appears to significantly amplify two erroneous peaks. There is a clear transitioning length between each of the elements layers where the spectra shows characteristic peaks belonging to both elements. This length is shortest for the transition between GaAs and Pd, and longest between Pd and Ge.

The resulting compositions from areas D and E in the heat-treated sample, using the ζ -factor method without absorption correction, are shown in Figs. 4.7 and 4.8 (++++ see Appendix X for equivalent maps from the CL-method and the ζ -method with absorption correction). The areas D and E are located, as seen in Figs. 4.7(a) and 4.8(a), in the melted region on the left and right side of the nanowire, respectively. The quantification for Figs. 4.7(b) to 4.7(e) and 4.8(b) to 4.8(e) was done with the assumption that the regions only contained Ga, As, Pd and/or Ge. The maps have been binned by a factor of two in the x- and y-directions, in order to reduce the effect of outlier values. Tables 4.2 and 4.3 provides a summary of the compositions of area D and E, respectively, in which the areas have been roughly divided into three regions: The inner region denotes the nanowire on the right side of area D and left side of area E, while the lower and upper regions are the lower, darker regions and the upper, brighter regions within the squares in Figs. 4.7(a) and 4.8(a), respectively.

Table 4.2: For area D (zeta)

Area	Ga	As	Ge	Pd	Au
Inner	45-55	45-55	0-3	0-5	-
Lower	3-10	3-10	25-40	50-65	0
Upper	10-15	10-15	10-20	65-73	0-2

Table 4.3: For area E (zeta)

Area	Ga	As	s Ge	Pd	Au
Inner 1	45-55	45-55	0-2	0-10	-
Lower 1	3-8	3-8	22-35	45-55	0-2
Upper 1	5-15	5-15	2-12	65-75	0-2

Fig. 4.9(a) shows three areas whose average compositions were calculated using all three techniques. As previously mentioned, it was not possible

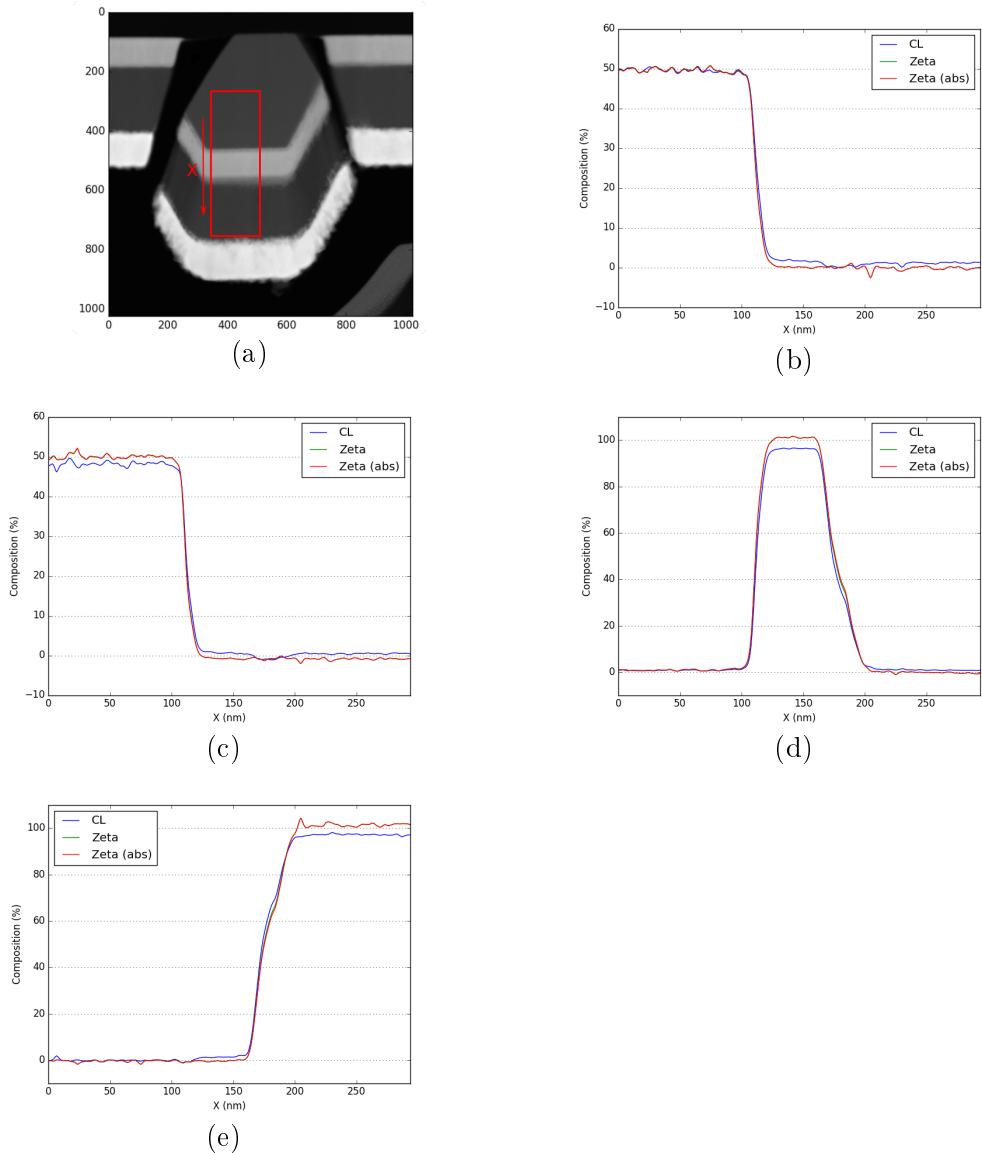


Figure 4.5: plots of....

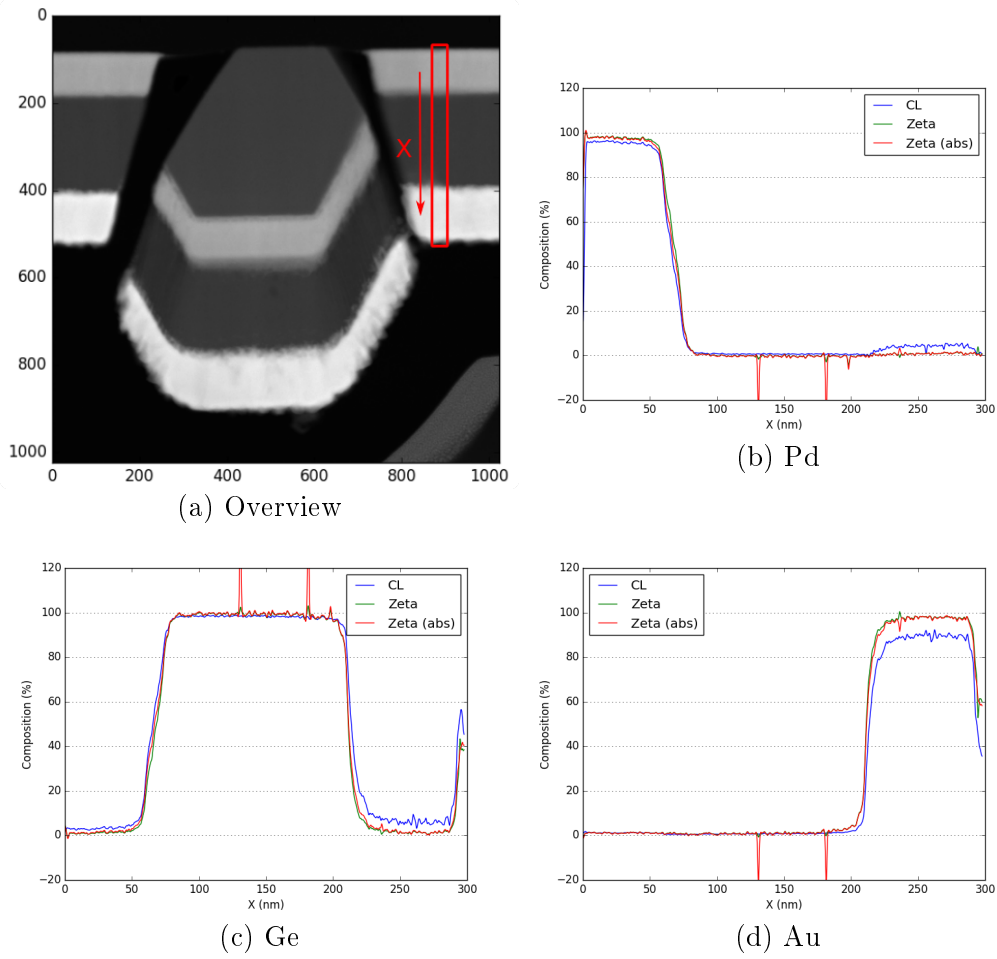


Figure 4.6: plots of....

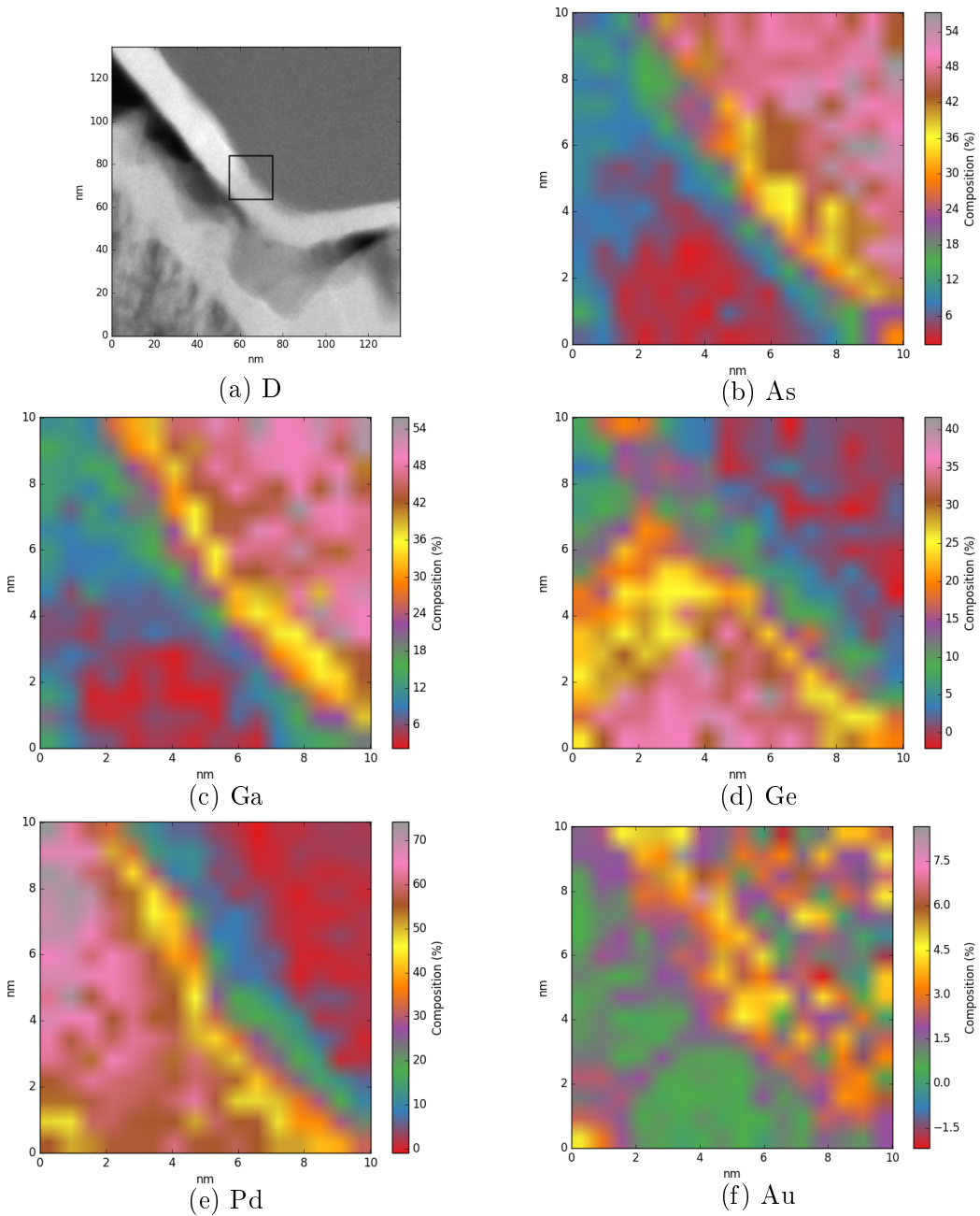


Figure 4.7: plots of....

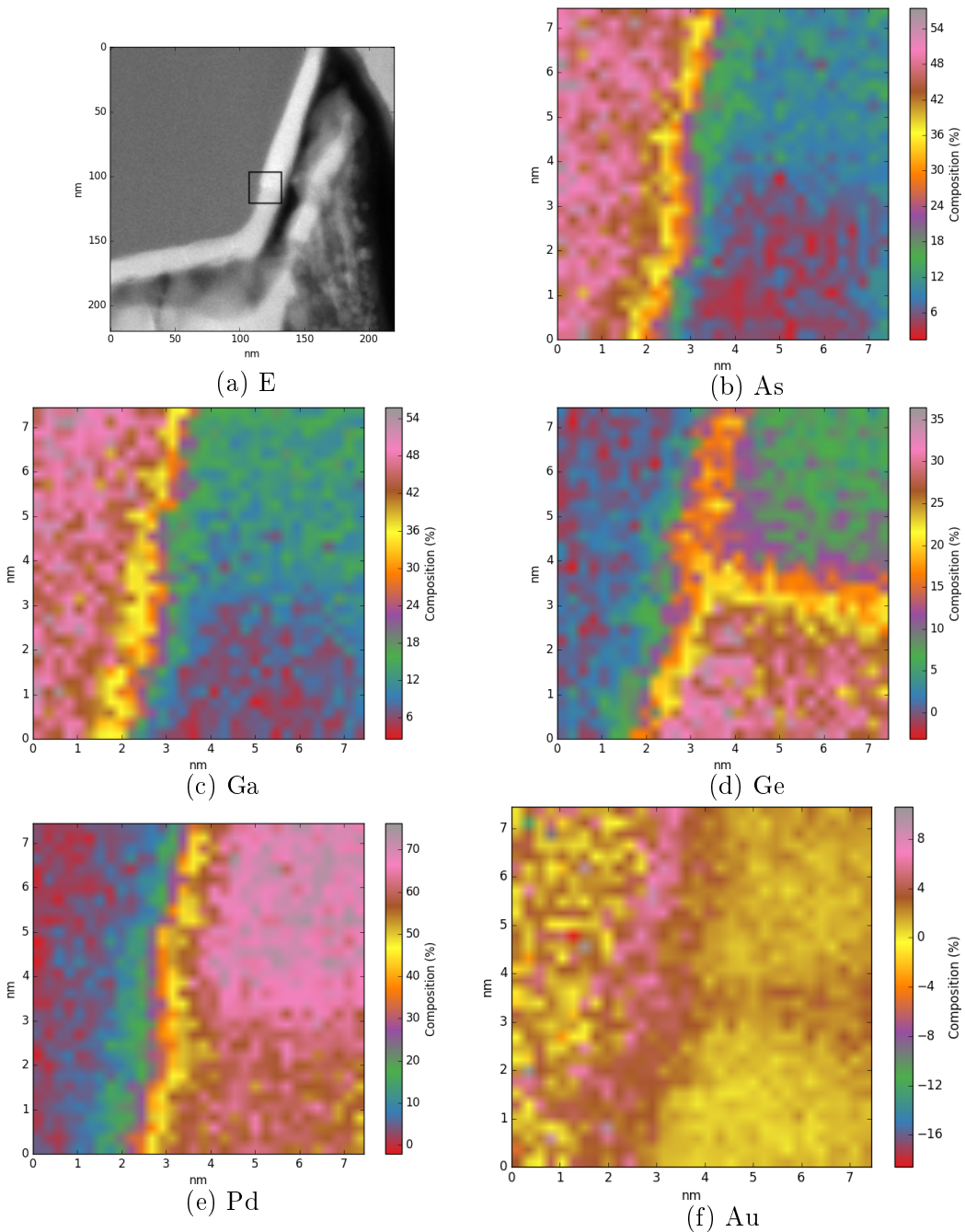
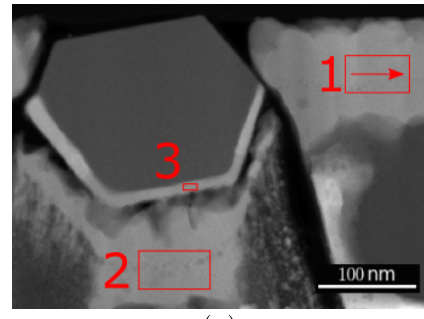


Figure 4.8: plots of....

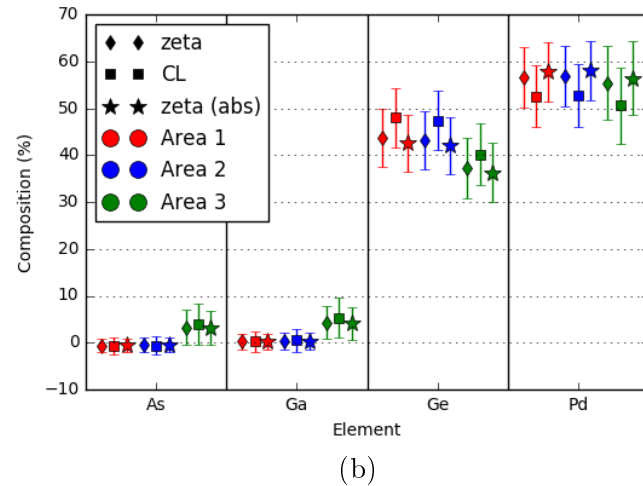
to calculate the composition of Au simultaneously with Ga and As, so two separate calculations were performed. Fig. 4.9(b) shows the results for Ga, As, Pd and Ge, while Fig. 4.9(c) includes only Pd, Ge and Au. The figures also shows the standard deviations of the calculated ζ -values.

It is clear from Fig. 4.9(b) that areas 1 and 2 contain no Ga or As, while area 3 contains about 5% of each, and the three different methods give very similar results for these elements. For Ge and Pd, the ζ -methods with and without absorption correction both give a composition of about 40-45 % Ge and 55-60 % Pd for areas 1 and 2, and 35-40% Ge and 55-60 % Pd for area 3. The CL-method results in approximately 5 pp more Ge and 5 pp less Pd in all areas, compared to the ζ -methods. The differences between the ζ -method with and without absorption correction are consistently only about 1-2 pp.

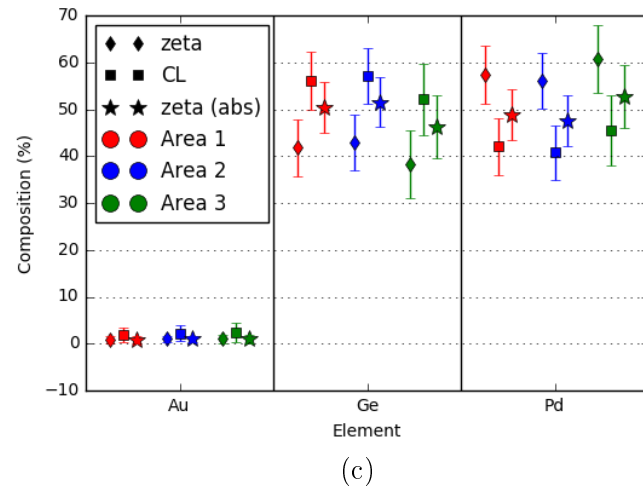
Fig. 4.9(c) gives slightly different results. It must here be noted that these results will be very inaccurate for area 3, which from Fig. 4.9(b) contains Ga and As, which is not included in this quantification process. However, areas 1 and 2, which do not contain Ga or As, ought to give the same compositions for Ge and Pd as before. Both ζ -methods now report little or no presence of Au in all areas, while the CL method gives a few percent. In areas 1 and 2, both the CL-method and the ζ -method with absorption correction reports that the ratios of Ge to Pd have been offset by up to more than 10 pp, compared to Fig. 4.9(b). On the other hand, the ζ -method without absorption gives approximately the same values for Ge and Pd; the Ge-to-Pd ratio has been skewed by a few percent at most.



(a)



(b)



(c)

Figure 4.9: Caption

Appendix A

Acronyms

FTA Fault tree analysis

MTTF Mean time to failure

RAMS Reliability, availability, maintainability, and safety

Appendix B

Additional Information

This is an example of an Appendix. You can write an Appendix in the same way as a chapter, with sections, subsections, and so on.

B.1 Introduction

B.1.1 More Details

Bibliography

- [1] E. Gullikson et.al. A. Thompson, D. Attwood. X-ray data booklet, 2001.
- [2] Thomas Aarholt. rotate. <https://github.com/thomasaarholt/hyperspy/tree/rotate>, 2016.
- [3] Francisco de la Peñsa, Tomas Ostasevicius, Vidar Tonaas Fauske, Pierre Burdet, Petras Jokubauskas, Mike Sarahan, Duncan Johnstone, Magnus Nord, Josh Taillon, Jan Caron, Katherine E. MacArthur, Alberto El-jarrat, Stefano Mazzucco, Tom Furnival, Eric Prestat, Michael Walls, Gaál Donval, Ben Martineau, Luiz Fernando Zagonel, Andreas Garmannslund, Thomas Aarholt, Christoph Gohlke, and iygr. hyperspy: Hyperspy 1.1.1, August 2016.
- [4] R.F. Egerton. *Electron Energy-Loss Spectroscopy in the Electron Microscope*. Springer, 2011.
- [5] Vidar Tonaas Fauske. Hyperspyui 0.6.1. <http://hyperspy.org/hyperspyUI/>, 2016.
- [6] G.W. Lorimer G. Cliff. Quantitative analysis of thin foils using emma-4 - the ratio technique. 1972.
- [7] Andreas Garmannslund. Refinement of the $\hat{\mu}$ -factor method for quantitative energy-dispersive x-ray spectroscopy in scanning transmission electron microscopy. Master's thesis, Norwegian University of Science and Technology, 2016.
- [8] D. B. Williams M. Watanabe. The quantitative analysis of thin specimens: a review of progress from the cliff-lorimer to the new ζ -factor methods. *Journal of Microscopy*, 221:89–109, 2 2006.

- [9] Kate MacArthur. linear_binning. https://github.com/k8macarthur/hyperspy/tree/Non_Integer_Binning, 2016.
- [10] Christopher Su-Yan Own. *System Design and Verification of the Precession Electron Diffraction Technique*. PhD thesis, 2005.
- [11] R. F. Egerton T. Malis, S. C. Cheng. Eels log ratio technique for specimen-thickness measurement in the tem. *Journal of Electron Microscopy Technique*, 8(2):193–200, 1988.
- [12] David B Williams and C. Barry Carter. *Transmission Electron Microscopy Part 1: Basics*. Springer, New York, 2009.